

Galactic Halos in MONDian Cosmological Simulations

Alexander Knebe and Brad K. Gibson

Centre for Astrophysics & Supercomputing, Swinburne University, P.O. Box 218, Mail # 31, Hawthorn, Victoria, 3122, Australia

Received ...; accepted ...

ABSTRACT

In this paper a series of high-resolution N -body simulations is presented in which the equations of motion have been changed to account for MODified Newtonian Dynamics (MOND). It is shown that a low- Ω_0 MONDian model with an appropriate choice for the normalisation σ_8 can lead to similar clustering properties at redshift $z = 0$ as the commonly accepted (standard) Λ CDM model. However, such a model shows no significant structures at high redshift with only very few objects present beyond $z > 3$ that can be readily ascribed to the low Ω_0 value adopted. The agreement with Λ CDM at redshift $z = 0$ is driven by the more rapid structure evolution in MOND. Moreover, galaxy formation appears to be more strongly biased in MONDian cosmologies. Within the current implementation of MOND density profiles of gravitationally bound objects at $z = 0$ can still be fitted by the universal NFW profile but MOND halos are less clumpy.

Key words: galaxy: formation – methods: N -body simulations – cosmology: theory – dark matter – large scale structure of Universe

1 INTRODUCTION

Although the currently favoured Λ CDM model has proven to be remarkably successful on large scales (cf. WMAP results, Spergel et al. 2003), recent high-resolution N -body simulations seem to be in contradiction with observation on sub-galactic scales: the Cold Dark Matter "crisis" on small scales is far from being over. The problem with the steep central densities of galactic halos, for instance, is still unsolved as the highest resolution simulations favor a cusp with a logarithmic inner slope for the density profile of approximately -1.2 (Power et al. 2003), whereas high resolution observations of low surface brightness galaxies are best fit by halos with a core of constant density (de Blok & Bosma 2002; Swaters et al. 2003). Suggested solutions to this include the introduction of self-interactions into collisionless N -body simulations (e.g. Spergel & Steinhardt 2000; Bento et al. 2000), replacing cold dark matter with warm dark matter (e.g. Knebe et al. 2002; Bode, Ostriker & Turok 2001; Colin et al. 2000) or non-standard modifications to an otherwise unperturbed CDM power spectrum (e.g. bumpy power spectra; Little, Knebe & Islam 2003; tilted CDM; Bullock 2001c). Some of the problems, as for instance the overabundance of satellites, can be resolved with such modifications but none of the proposed solutions have been able to rectify *all* shortcomings of Λ CDM simultaneously.

Therefore, there might be alternative solutions worthy of exploration, one of which is to abandon dark matter completely and to adopt the equations of MODified Newtonian Dynamics (MOND; Milgrom 1983; Bekenstein & Milgrom

1984). It has already been shown by other authors that this simple idea might explain many properties of galaxies without the need of non-baryonic matter (e.g. Scarpa 2003; McGaugh & de Blok 1998; Sanders 1996; Milgrom 1994; Begeman, Broeils & Sanders et al. 1991). MOND is also successful in describing the dynamics of galaxy groups and clusters (Sanders 1999; Milgrom 1998), globular clusters (Scarpa 2002) and, to a limited extent, gravitational lensing (Mortlock & Turner 2001; Qin & Zou 1995). A recent review of MOND is given by Sanders & McGaugh (2002) which also summarizes (most of) the successes alluded to above.

However, there has yet to come a detailed study of the implications of MOND in cosmological simulations of structure and galaxy formation, which is the aim of the current study. Nusser (2002) already investigated modified Newtonian dynamics of the large-scale structure using the N -body approach. His simulations, however, are lower resolution, both in terms of spatial and mass resolution, making a study of individual objects difficult. Moreover, his implementation of the MOND equations is slightly different to our treatment.

The outline of the paper is as follows. In Section 2 we present the way we modified our N -body code MLAPM to account for MOND. Section 3 introduces the cosmological models under investigation whereas Section 4 summarizes the numerical details. The analysis can be found in Section 5. We finish with a summary and our conclusions in Section 6.

2 THE MONDIAN EQUATIONS OF MOTION

In an N -body code one integrates the (comoving) equations of motion

$$\begin{aligned}\dot{\vec{x}} &= \frac{\vec{p}}{a^2}, \\ \dot{\vec{p}} &= \frac{\vec{F}_{\text{pec}}}{a}\end{aligned}\quad (1)$$

which are completed by Poisson's equation

$$\vec{\nabla}_x \cdot \vec{F}_{\text{pec}}(\vec{x}) = -\Delta_x \Phi(\vec{x}) = -4\pi G(\rho(\vec{x}) - \bar{\rho}). \quad (2)$$

In these equations $\vec{x} = \vec{r}/a$ is the comoving coordinate, \vec{p} the canonical momentum, $\vec{\nabla}_x$ the divergence operator (Δ_x the Nabla operator) with respect to \vec{x} and $\vec{F}_{\text{pec}}(\vec{x}) = -\nabla\Phi(\vec{x})$ the *peculiar acceleration field in comoving coordinates*. We now need to modify these (comoving) equations to account for MOND.

Despite MOND being a modification to Newton's second law rather than to gravity, one has the option to actually interpret MOND as an alteration of the law of gravity (cf. Sanders & McGaugh 2002). In that case Poisson's equation

$$\vec{\nabla}_r \cdot \vec{g} = -4\pi G\rho(\vec{r}) \quad (3)$$

is replaced by

$$\vec{\nabla}_r \cdot (\mu(|\vec{g}_M|/g_0) \vec{g}_M) = -4\pi G\rho(\vec{r}), \quad (4)$$

where $\vec{r} = a\vec{x}$ is the proper coordinate, g_0 the fundamental acceleration of MOND and \vec{g}_M the MONDian acceleration field. Note that Eq. (3) and Eq. (4) are given in proper coordinates in contrast to Eq. (2) where the solution \vec{F}_{pec} describes only the *peculiar* acceleration.

If we now compare Eq. (3) and Eq. (4) we find the relation between MONDian acceleration g_M and Newtonian acceleration g to be:

$$\vec{g} = \mu(\vec{g}_M/g_0)\vec{g}_M + \nabla \times \vec{h}. \quad (5)$$

The field equation (4) is non-linear and difficult to solve in general. But it has been shown by Bekenstein & Milgrom (1984) that $\nabla \times \vec{h}$ decreases like $\mathcal{O}(r^{-3})$ with increasing scale. Moreover, in cases of spherical, planar, or cylindrical symmetry the curl-term vanishes. Under the assumption that objects forming in the Universe show at least one of these symmetries we are able to neglect the curl-term completely. One might argue that this kind of symmetry is probably very weak at high redshifts. However, later in this Section we are also making the assumption that MOND only affects peculiar accelerations (in proper coordinates) which are well above the MOND acceleration at early times (cf. Eq. (12)). We therefore presume that $\nabla \times \vec{h}$ is unimportant for the growth of large-scale structures as well as for the internal properties of virialized objects (under the assumption that they are at least symmetric along one of their axes).

Using Milgrom's (1983) suggested interpolation function

$$\mu(x) = x(1+x^2)^{-1/2} \quad (6)$$

one now only needs to solve

$$g_M^2 - g\sqrt{g_0^2 + g_M^2} = 0, \quad (7)$$

to get g_M as a function of g . The relevant solution of Eq. (7) is

$$g_M = g \left(\frac{1}{2} + \frac{1}{2} \sqrt{1 + \left(\frac{2g_0}{g} \right)^2} \right)^{1/2}. \quad (8)$$

Eq. (8) allows us to obtain the MONDian acceleration \vec{g}_M for a given Newtonian acceleration \vec{g} where \vec{g}_M and \vec{g} are assumed to be parallel.

However, we are actually solving Eq. (2) in our N -body code **MLAPM** which gives \vec{F}_{pec} , the Newtonian peculiar acceleration in *comoving coordinates*. Therefore, we also need to derive a relation between the proper acceleration $\vec{g} = \ddot{\vec{r}}$, the proper peculiar acceleration \vec{g}_{pec} , and the peculiar acceleration in comoving coordinates \vec{F}_{pec} . The second derivative with respect to time of $\vec{r} = a\vec{x}$ gives

$$\ddot{\vec{r}} = a\ddot{\vec{x}} + 2\dot{a}\dot{\vec{x}} + \ddot{a}\vec{x}, \quad (9)$$

whereas combining Eqs. (1) leads to

$$\ddot{\vec{x}} + 2\frac{\dot{a}}{a}\dot{\vec{x}} = \frac{\vec{F}_{\text{pec}}}{a^3} \quad (10)$$

Using the second Friedmann equation we can then rewrite Eq. (9) as follows

$$\ddot{\vec{r}} = \frac{1}{a^2} \left(\vec{F}_{\text{pec}} - \frac{4\pi G}{3} \bar{\rho} \vec{x} \right). \quad (11)$$

This equation shows that the *peculiar acceleration in proper coordinates* \vec{g}_{pec} should be defined as

$$\vec{g}_{\text{pec}} = \vec{F}_{\text{pec}}/a^2 \quad (12)$$

where \vec{F}_{pec} is the solution of Poisson's equation Eq. (2) as obtained by **MLAPM**.

If we now make the assumption that MOND *only* affects the peculiar acceleration in proper coordinates but leaves the Hubble acceleration unchanged, the recipe for getting the MONDian peculiar accelerations in comoving coordinates $\vec{F}_{M,\text{pec}}$ is as follows:

- (i) solve Eq. (2) using **MLAPM** which gives \vec{F}_{pec}
- (ii) use Eq. (12) to transfer \vec{F}_{pec} to $\vec{g}_{\text{pec}} = \vec{F}_{\text{pec}}/a^2$
- (iii) use Eq. (8) to calculate $\vec{g}_{M,\text{pec}}$ from \vec{g}_{pec}
- (iv) transfer $\vec{g}_{M,\text{pec}}$ back to $\vec{F}_{M,\text{pec}} = a^2 \vec{g}_{M,\text{pec}}$
- (v) use $\vec{F}_{M,\text{pec}}$ rather than \vec{F}_{pec} in Eq. (1)

This scheme has been employed for the simulations carried out with **MLAPM** described below*. We like to point out that our treatment of MOND agrees with the one advocated by Sanders (2001) in the limit $\beta = 0$.

3 THE COSMOLOGICAL MODELS

The reason for introducing MOND by Milgrom (1983) was to explain the flat rotation curves of galaxies *without* the need for dark matter. Having this in mind we decided to use an Ω_0 value for the MOND simulation that is close to the upper bound allowed by Big-Bang-Nucleosynthesis and agrees with the recent measurements of cosmological parameters by the WMAP experiment (Spergel et al. 2003). Our database of simulations is made up of the following three runs

* The latest release version of **MLAPM** includes the MOND implementation which can be activated using `-DMOND` on compile time.

Table 1. Model parameters. In all cases a value for the Hubble parameter of $h = 0.7$ was employed.

label	Ω_0	Ω_b	λ_0	$\sigma_8^{z=0}$	σ_8^{norm}	g_0 [cm/s ²]
Λ CDM	0.30	0.04	0.7	0.88	0.88	—
OCBM	0.04	0.04	0.0	0.88	0.88	—
OCBMond	0.04	0.04	0.0	0.92	0.40	1.2×10^8

- a standard Λ CDM model,
- an open, low- Ω_0 model with the same σ_8 as Λ CDM,
- an open, low- Ω_0 model with MOND and adjusted σ_8 .

These runs are labeled Λ CDM, OCBM and OCBMond, respectively, and their cosmological parameters are summarized in Table 1. The OCBM model is only to be understood as a gauge for the MOND model run rather than an alternative to Λ CDM.

We can see from Eq. (12) that the peculiar accelerations (which are subject to MOND) are large at early times and therefore a "Newtonian treatment" in the early universe is justified. Therefore, the input power spectra to our initial conditions generator were calculated using the CMBFAST code (Seljak & Zaldarriaga 1996) with $\Omega_0 = \Omega_b = 0.04$ for OCBM and OCBMond, respectively. This explains the choice for using the expression CBM rather than CDM. Such a relatively high Ω_b value (compared to Ω_0) actually introduces "baryon wiggles" into the primordial power spectrum (oscillations frozen into the plasma at the epoch of recombination which are suppressed in dark matter dominated models). However, fluctuations on scales of the box size employed ($B = 32h^{-1}$ Mpc, see below) and smaller are not affected by it other than an overall "damping" (e.g. Eisenstein & Hu 1998; Silk 1968). This damping, however, is compensated by the choice of normalisation σ_8^{norm} of the power spectrum. We, moreover, differentiate between σ_8^{norm} and the actual measure of $\sigma_8^{z=0}$ in the simulations at redshift $z = 0$ because the OCBMond model requires a lower $P(k)$ -normalisation σ_8^{norm} to arrive at a comparable $\sigma_8^{z=0}$ value. This is due to a much faster growth of structures when using MOND which will be emphasized in more detail in Section 5.

4 THE N-BODY SIMULATIONS

Using the input power spectra derived with the CMBFAST code we displace 128^3 particles from their initial positions on a regular lattice using the Zel'dovich approximation (Efsthathiou, Frenk & White 1985). The box size was chosen to be $32h^{-1}$ Mpc on a side. This choice guarantees proper treatment of the fundamental mode which will still be in the linear regime at $z = 0$ (cf. the scale turning non-linear at $z = 0$ is roughly $20h^{-1}$ Mpc for the models under investigation). The particles were evolved from redshift $z = 50$ until $z = 0$ with the open source adaptive mesh refinement code MLAPM (Knebe, Green & Binney 2001). We employed 500 steps on the domain grid built of 256^3 cells, and in all three runs a force resolution of $11h^{-1}$ kpc was reached in the highest density regions. The mass resolution of the runs is $m_p = 1.30 \cdot 10^9 h^{-1} M_\odot$ for the Λ CDM model and $m_p = 0.17 \cdot 10^9 h^{-1} M_\odot$ for the two low- Ω_0 models, respectively. We output the particle positions and velocities at redshifts $z = 5, 3, 1, 0.5$, and 0. These "snapshots" are

then analysed with respect to the large-scale clustering as well as properties of individual objects. And even though in OCBM(ond) we made the assumption of the non-existence of dark matter we still refer to these objects as "halos"; due to the absence of dissipation they show similar shapes and density distributions when being compared to their Λ CDM counterparts as can be seen in the analysis below.

Gravitationally bound objects are identified using the Bound-Density-Maxima method (BDM, Klypin & Holtzman 1997). The BDM code identifies local overdensity peaks by smoothing the density field on a particular scale of the order of the force resolution. These peaks are prospective halo centres. For each of these halo centers we step out in (logarithmically spaced) radial bins until the density reaches $\rho_{\text{halo}}(r_{\text{vir}}) = \Delta_{\text{vir}} \rho_b$ where ρ_b is the background density. This defines the outer radius r_{vir} of the halo. However, one needs to carefully choose the correct virial overdensity Δ_{vir} which is much higher for the OCBM and OCBMond model due to the low Ω_0 value. The parameters used are $\Delta_{\text{vir}} = 340$ for Λ CDM and $\Delta_{\text{vir}} = 2200$ for OCBM/OCBMond (see Gross 1997, Appendix C, and references therein).

Brada & Milgrom (1999) raised the issue that care should be taken when numerically integrating the equations of motion using MOND. Even more so in our case where we made the assumption that the curl-term in Eq. (5) vanishes which gives rise to forces that are not strictly conservative. We therefore performed a simple test on the final output to assure that our implementation of MOND does not violate momentum conservation: the net momentum of all particles in the box as well as the net force should vanish. We calculated the following sums

$$\left| \sum_i \vec{v}_i \right| = C_1 \sum_i |\vec{v}_i|, \quad \text{and} \quad \left| \sum_i \vec{F}_i \right| = C_2 \sum_i |\vec{F}_i|, \quad (13)$$

and derived values for C_1 and C_2 in all three models. In Λ CDM and OCBM those constants $C_{1,2}$ are of the order 10^{-4} and even though in OCBMond they are about an order of magnitude larger we still believe that they are sufficiently small. It has been shown elsewhere (Knebe, Green & Binney 2001) that adaptive softening in general does not guarantee precise momentum conservation and our values for C_1 and C_2 are as expected.

5 ANALYSIS

5.1 Large-Scale Clustering Properties

We start with inspecting the large-scale density field in all three runs. Fig. 1 shows a projection of the whole simulation with each individual particle grey-scaled according to the local density at redshift $z = 0$ and $z = 5$. This figure indicates that the MOND simulation looks fairly similar to the other two models in terms of the locations of high density peaks (dark areas), filaments and the large-scale structure, respectively. One should bear in mind though that the OCBMond simulation was started with a much lower σ_8^{norm} normalisation than the other two runs. This is in fact reflected in the right panel showing the density field at redshift $z = 5$; the MOND simulation is less evolved. Moreover, without any further analysis one might even be inclined to conclude

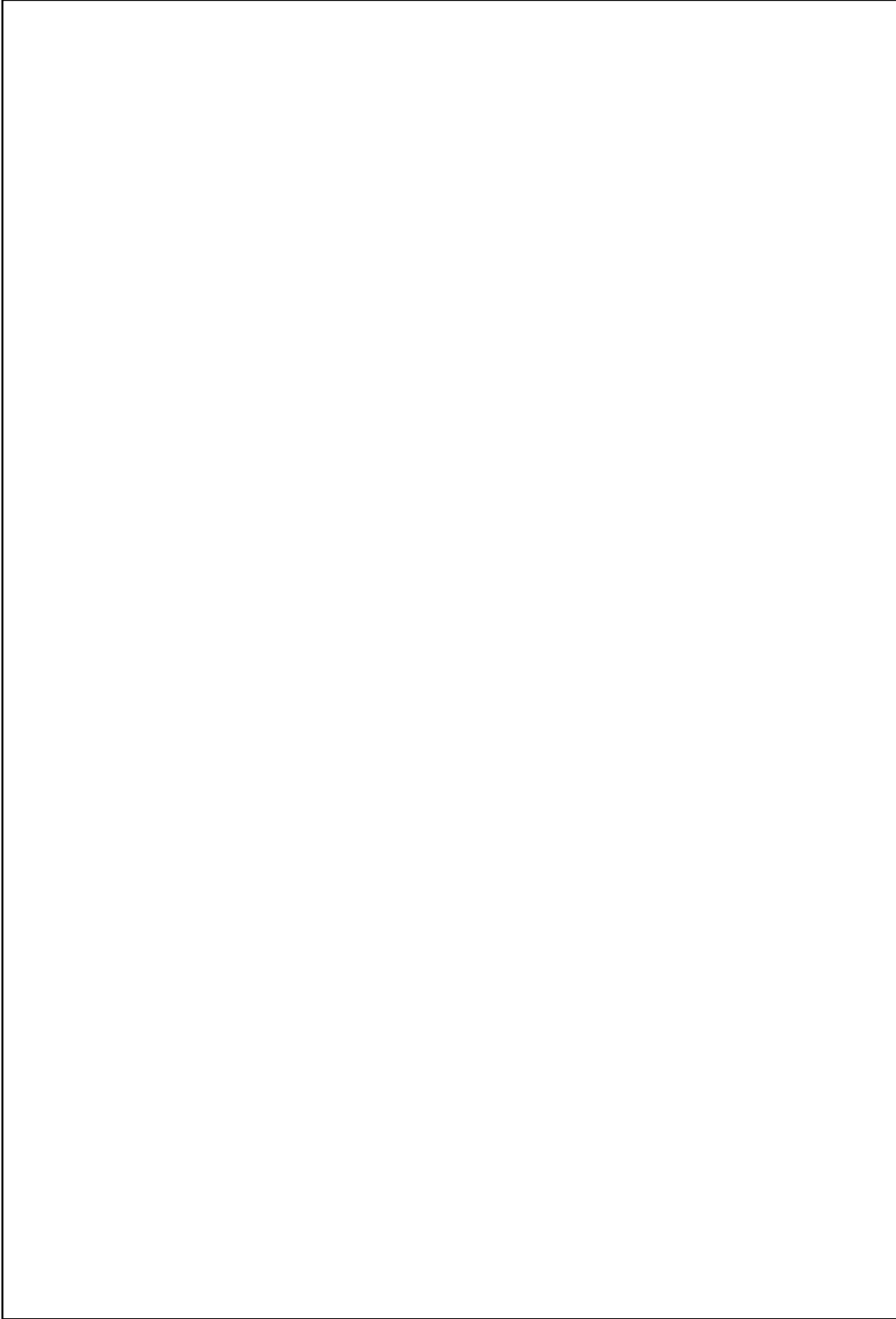


Figure 1. Comparison of the large-scale density field of the three models under investigation at redshift $z = 0$ (left) and $z = 5$ (right). The upper panel shows the Λ CDM simulation, the middle panel the OCBMond model and the lower one OCBM.

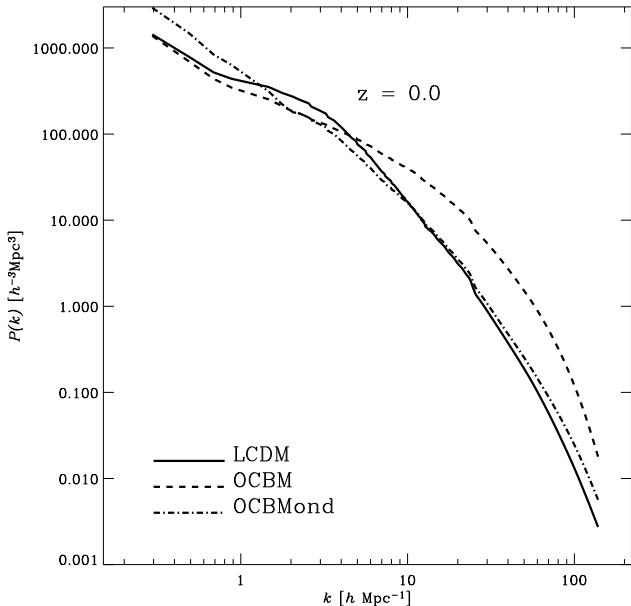


Figure 2. Matter power spectra for all three model at redshift $z = 0$ (thick lines) and $z = 5$ (thin lines).

from Fig. 1 that the MOND model is more strongly clustered at $z = 0$ which is affirmed by the slightly higher $\sigma_8^{z=0}$ value given in Table 1. But as we will see later on this is not necessarily true; we can confirm a higher amplitude of the two-point correlation function for galaxies in OCBMond (cf. Fig. 5) while at the same time showing a comparable amplitude in the matter power spectrum on small scales. The latter can be viewed in Fig. 2 where we plot the matter power spectrum for all three models at redshift $z = 0$. There we observe that the OCBMond model shows a slightly larger amplitude for $k < 0.8 h \text{Mpc}^{-1}$ (scales close to the fundamental mode). Nusser (2002), who treated the MOND equation similarly (but differently) to us[†], already pointed out that the linear evolution of the growing mode solution for the density contrast δ scales like $\delta \propto a^2$ as opposed to Newtonian theory where $\delta \propto a$. This explains why the OCBMond model with the (initially) low σ_8^{norm} normalisation outruns the evolution of the Newtonian OCBM simulation. In other words, the MOND model had to be started with a lower σ_8 normalisation to provide competitive results at redshift $z = 0$. Sanders (2001) also noted that due to a much faster growth of structures in MOND universes the amplitude of $P(k)$ for purely baryonic models matches the standard ΛCDM cosmology. We also like to point out that the required value $\sigma_8^{\text{norm}} = 0.4$ needed to bring the MOND simulation into agreement with the standard ΛCDM model is closer to the COBE normalisation $\sigma_8^{\text{COBE}} \approx 0.1$ for that particular cosmology. Another feature worth noting is that the OCBMond power spectrum does not show a distinctive “break” due to the transfer of power from large to small scales as seen in both the ΛCDM and the OCBM model.

[†] Nusser (2002) did not use Milgrom’s interpolation function as given by Eq. (6) but rather a spontaneous transition from Newtonian to MOND accelerations.

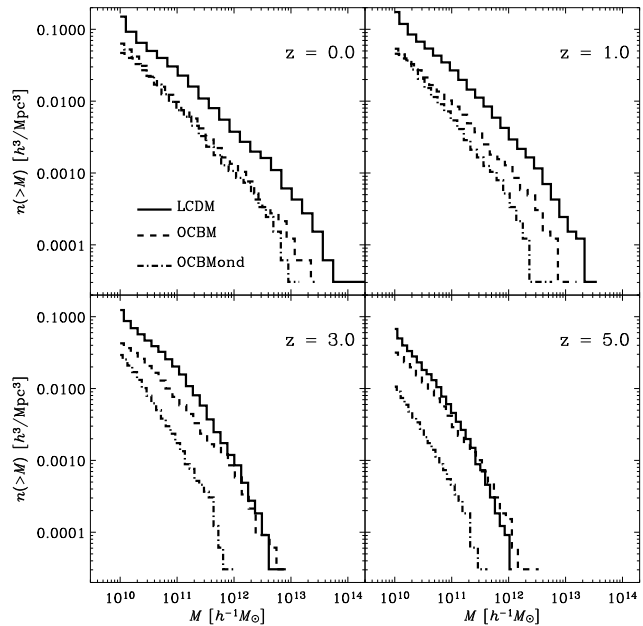


Figure 3. Cumulative mass function for all three models at redshifts $z = 5, 3, 1$ and 0 .

In Fig. 3 we are plotting the cumulative mass function of objects identified using the BDM technique (Klypin & Holtzmann 1997). This figure highlights again that the hierarchical formation of gravitationally bound objects is driven much faster in the MOND simulation but being initiated at later times. At a redshift of $z = 5$ we can see that the abundance of objects on all mass scales is nearly identical in the OCBM and ΛCDM model with a much lower amplitude for OCBMond. Whereas the evolution for the Newtonian OCBM run already ceases at a redshift of around $z_{\text{stop}} \simeq 1/\Omega_0 - 1 \simeq 24$ we still see a very strong increase (by more than one order of magnitude) in the number density of objects of all masses in the OCBMond simulation. To emphasize on this, Fig. 4 shows the (integral) abundance evolution of objects with mass $M > 10^{11} h^{-1} M_\odot$. The OCBM model undoubtedly experiences very little evolution from $z \sim 5$ to today whereas both other models show a very steep evolution. The discrepancy between the OCBMond and the other two models at redshift $z = 5$ can, however, be ascribed to the lower initial σ_8^{norm} value though; OCBMond was set up with much smaller initial density perturbation which only grew to a comparable level of clustering via the effects of MOND. This is again in agreement with the findings of Sanders (2001) who showed that the collapse of spherically symmetric overdensities becomes MOND dominated for redshifts $z \lesssim 5$ and hence starts to outrun Newtonian models (cf. Fig.5 in Sanders 2001).

The question now arises to what degree the (formation) sites of halos in ΛCDM and the two OCBM models are correlated. To this extent we calculated the two-point correlation function of the 500 most massive objects and the result can be found in Fig. 5. We chose to use a fixed number of halos rather than a mass cut for the calculation of $\xi_{\text{gal}}(r)$ in order not to introduce an artificial bias. We do have far more objects of a given mass in the ΛCDM model and therefore a mass limit M_{min} used with the estimator for $\xi_{\text{halo}}(r)$ would

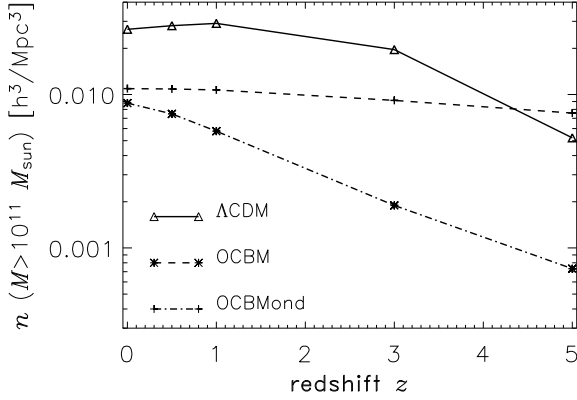


Figure 4. Redshift evolution of the abundance of halos with mass $M > 10^{11} h^{-1} M_{\odot}$.

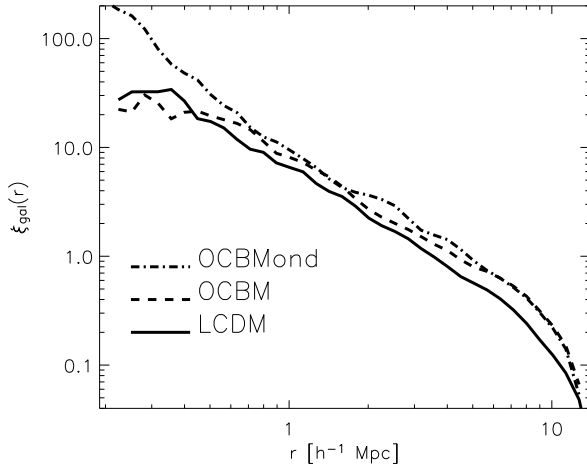


Figure 5. Two-point correlation function at redshift $z = 0$ for the 500 most massive objects.

lead to different correlation amplitudes. The agreement between the Newtonian OCBM and the Λ CDM model is not surprising. As already pointed out by other authors, the correlation function is expected to be (nearly) identical in cases of equal σ_8 normalizations, irrespective of the cosmological model (Martel & Matzner 2000). Moreover, if the model is fixed and only the σ_8 normalization varied it should leave no imprint on $\xi_{\text{gal}}(r)$ (Croft & Efstathiou 1994). But the OCBMond model stands out again having a much higher amplitude on all scales. This clearly attributes for the differences already mentioned in the discussion of Fig. 1 and indicates that the OCBMond model is more evolved at redshift $z = 0$ than the other two models even though the matter power spectrum has a lower amplitude on corresponding scales: structure formation in MONDian cosmologies is even more biased than in Newtonian models. This is in agreement with findings that small scales enter the MOND regime before large-scale fluctuations (cf. Nusser 2002; Sanders 2001).

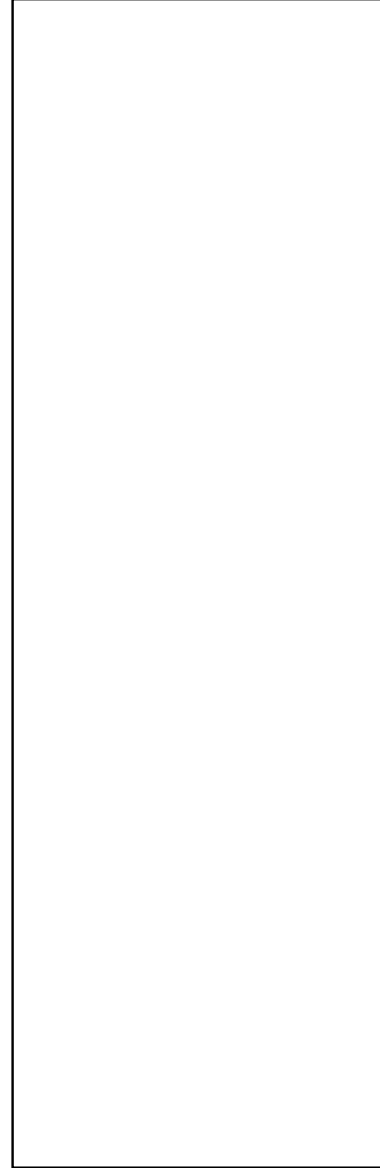


Figure 6. Most massive galactic halo in Λ CDM (upper panel), OCBMond (middle panel) and OCBM (lower panel). The line in the lower right corner of each panel is a scale indicating $100 h^{-1} \text{ kpc}$.

5.2 Galactic Halos

Having analysed the large-scale clustering properties we now turn to the investigation of the internal properties of galactic halos. To this extent we use the halo catalogues based on the BDM code (Klypin & Holtzmann 1997) and neglecting objects less massive than $M < 10^{11} h^{-1} M_{\odot}$ again. This sets the minimum number of particles per halo to 77 for Λ CDM and 488 for OCBM(ond).

A visualization of the density fields throughout the most massive BDM halo is given in Fig. 6. It is quite striking that neither of the low- Ω_0 halos shows substantial substructure. However, this is easily understood for OCBM, because in a low-density universe structure formation ceases at early times ($z_{\text{stop}} \simeq 1/\Omega_0 - 1$). This means that clusters in such cosmologies should show fewer substructure since they had

more time to virialize (cf. Knebe & Müller 2000). But this explanation obviously does not hold for OCBMond as nearly all halos in that particular model formed exceptionally late (cf. Fig. 4).

The most interesting question, however, is probably the shape of the density profile and the rotation curve for halos in MONDian cosmologies, respectively. Fig. 7 now shows the matter profile of the most massive halo in all three models along with fits (thin solid lines) to a Navarro, Frenk & White (NFW) profile (Navarro, Frenk & White 1997)

$$\rho_{\text{NFW}}(r) \propto \frac{1}{r/r_s(1+r/r_s)^2}. \quad (14)$$

The scale radius r_s is being used to define the concentration of the halo $c = r_{\text{vir}}/r_s$ where r_{vir} is the radius at which the density reaches the virial overdensity $\Delta_{\text{vir}} \approx 340$ and $\Delta_{\text{vir}} \approx 2200$ for Λ CDM and OCBM(ond), respectively.

We observe that even for the OCBMond model the data is equally well described by the functional form of a NFW profile (out to the virial radius, at least). However, the central density of that halo in the OCBMond model is lower than in Λ CDM and especially in OCBM. The high central density for OCBM is readily explained by the fact that halos in that particular cosmology form at a time when the universe is still very dense. This result is also supported by the values of the concentration parameter presented in Table 2: the most massive object in the MOND model shows the lowest concentration c , mostly due to the late onset of formation as observed in Fig. 4. When inverting the density profile into a (Newtonian) circular velocity curve by simply using $v_{\text{circ}}^2(r) = GM(<r)/r$, this also entails a shift of the maximum of the rotation curve to higher radii as can be seen in Fig. 8 ($r_{\text{max}}^{\text{circ}} \approx 2r_s$, Navarro, Frenk & White 1997). The functional shape of the rotation curves for an NFW density profile is given by

$$\frac{v_{\text{circ}}^2}{v_{\text{vir}}^2} = \frac{1}{x} \frac{\ln(1+cx) - (cx)/(1+cx)}{\ln(1+c) - c/(1+c)} \quad (15)$$

with v_{vir} being the (Newtonian) circular velocity at the virial radius r_{vir} and $x = r/r_{\text{vir}}$. The drop of the maximum of the rotation curve by about a factor of 3.2 is merely a reflection of the scatter in mass for the most massive halo throughout the three models. As can be seen in Table 2 the halo is more than ten times as massive in Λ CDM than in OCBMond. This should give an about 2.7 times higher $v_{\text{max}}^{\text{circ}}$ as the scaling between those two quantities is roughly $v_{\text{max}}^{\text{circ}} \propto M_{\text{vir}}^{1/3}$. This scaling relation can be derived when using $x_{\text{max}}^{\text{circ}} \approx 2/c$ (cf. Bullock et al. 2001b and Navarro, Frenk & White 1997) together with Eq. (15) giving

$$v_{\text{circ}}^{\text{max}} \propto v_{\text{vir}} \sqrt{\frac{c}{\ln(1+c) - c/(1+c)}} \quad (16)$$

If we furthermore assume $c \propto M^{-0.13}$ as shown by Bullock et al. (2001b, cf. Eq(18)) we find that the $\sqrt{\dots}$ -factor in Eq. (16) is roughly constant for the mass range under consideration. And as $v_{\text{vir}} \propto M^{1/3}$ (which simply follows from $v^2 \propto M/r$ and $r \propto M^{1/3}$ for a spherical overdensity) the same scaling then holds for $v_{\text{circ}}^{\text{max}}$ explaining the observed drop of the maximum of the rotation curve for the OCBMond model.

However, for the OCBMond model we should take into account that accelerations are *not* Newtonian and hence

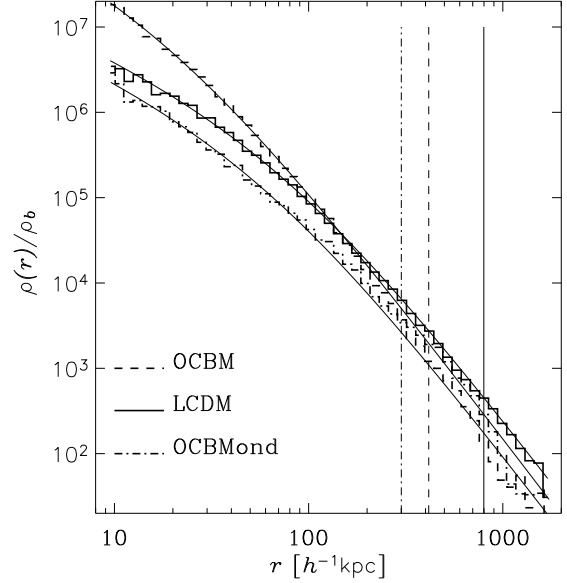


Figure 7. Density profile for the most massive halo in all three models. The vertical thin lines are indicating the virial radii.

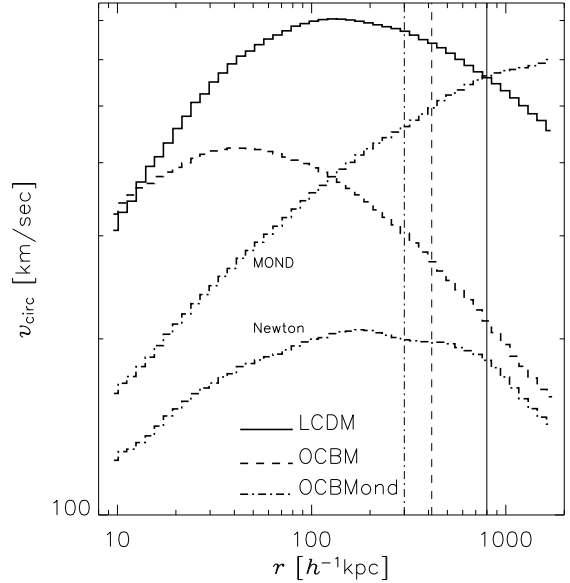


Figure 8. Rotation curve of the most massive halo.

$v_{\text{circ}}^2(r) = GM(<r)/r$ does not hold. Therefore we also show in Fig. 8 the actual MONDian rotation curve calculated as follows: the Newtonian acceleration $g = v^2/r$ is transferred to the MONDian acceleration g_M according to Eq. (8). g_M in turn is used to calculate $v_M(r) = \sqrt{g_M r}$. The resulting $v_{\text{circ}}(r)$ is labelled "MOND" in Fig. 8. We note that the MONDian velocities are actually larger than the Newtonian ones bringing them closer to the Λ CDM model. This has implications for dynamical mass estimates of galaxy clusters as presented in Sanders (1999). Sanders showed that the dynamically estimated mass of galaxy clusters is too

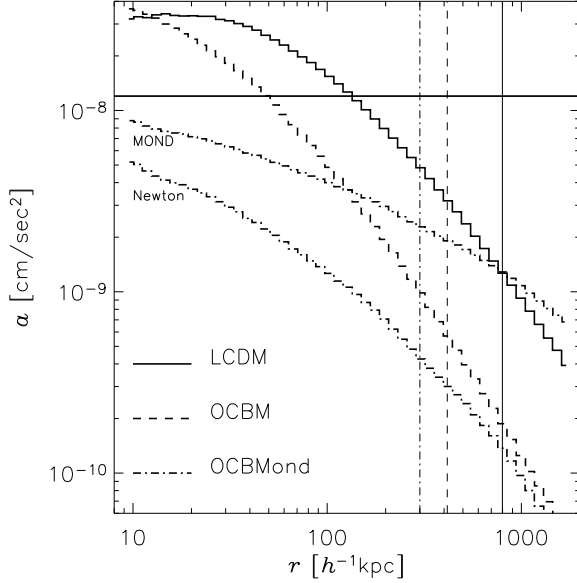


Figure 9. Acceleration curve of the most massive halo. The solid vertical line indicates the MONDian acceleration parameter $g_0 = 1.2 \times 10^8 \text{cm/sec}^2$.

large compared to the observed mass when using Newtonian physics. However, MOND rectifies dynamical masses bringing them into better agreement with observed masses. And a similar phenomenon can be observed in Fig. 8: the MONDian curve for OCBMond would be measured observationally and hence be translated into a too high cluster mass of $M_{\text{vir}} \approx 2.8 \cdot 10^{13} h^{-1} M_{\odot}$ when using Newtonian dynamics. MOND, on the contrary, would give the real value of $M_{\text{vir}} = 0.3 \cdot 10^{13} h^{-1} M_{\odot}$. Later on we will see that this leaves an imprint on the (radial) distribution of the spin parameter, too.

In addition to the rotation curve we also show the acceleration as a function of radius in Fig. 9. The object that formed in OCBMond has MONDian accelerations throughout the whole halo whereas the central parts of the objects in the other two models are above the universal acceleration g_0 indicated by the thin solid line.

We like to stress that in both Figs 7 and 8 the Newtonian curves for the OCBMond model are only plotted for completeness; they do *not* carry observable information as the halo actually follows MONDian physics rather than Newtonian. However, they are educational in a sense to gauge the importance MOND has on the internal structure of the halo.

Table 2 now lists some internal properties in addition to the ones already mentioned, i.e. the velocity dispersion σ_v , the virial radius r_{vir} , the triaxiality T , ellipticities e_1 and e_2 , the spin parameter λ as well as best-fit parameters λ_0 and σ_{λ} when fitting the probability distribution $P(\lambda)$ to a log-normal distribution. The spin parameter λ was calculated using the definition given in Bullock et al. (2001a)

$$\lambda = \frac{J}{\sqrt{2} M_{\text{vir}} v_{\text{vir}} r_{\text{vir}}}, \quad (17)$$

which proved to be a more stable measurement than the

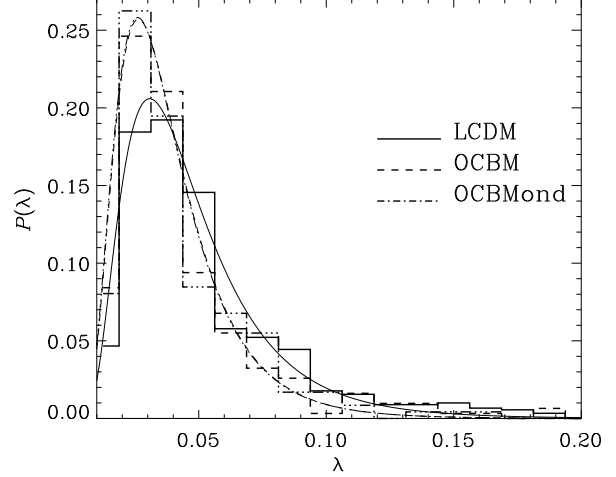


Figure 10. Spin parameter distribution in all three models. Lines show fits obtained using the log-normal distribution given by Eq. (18).

usual $\lambda' = J\sqrt{|E|}/(GM^{5/2})$ definition. For the OCBMond model v_{vir} is again the MONDian circular velocity at the virial radius. The distribution of λ , $P(\lambda)$, has been fitted to a log-normal distribution (e.g. Frenk et al. 1988; Warren et al. 1992; Cole & Lacey 1996; Maller, Dekel & Somerville 2002; Gardner 2001)

$$P(\lambda) = \frac{1}{\lambda\sqrt{2\pi}\sigma_0} \exp\left(-\frac{\ln^2(\lambda/\lambda_0)}{2\sigma_0^2}\right). \quad (18)$$

The results are presented in Fig. 10 showing that the OCBMond distribution $P(\lambda)$ is nearly indistinguishable from the other two models. However, the reduced χ^2 value for OCBMond is about a factor of two larger (cf. Table 2). As been noted by Maller, Dekel & Somerville (2001) the log-normal distribution given by Eq. (18) is not as good a fit to models with halos that are recent merger remnants. This is definitely one of the effects that has an influence on the spin parameter distribution for the OCBMond model as we expect a high level of recent merger activity (cf. Fig. 4).

We also calculated the radial distribution of $\lambda(< r)$ throughout the halos and present the result for the most massive one in Fig. 11. We see that $\lambda(< r)$ is roughly constant for the Newtonian models of structure formation whereas there is a sharp increase of $\lambda(< r)$ in the MOND halo towards the virial radius. This implies that the material in that particular halo moves on more circular orbits and the object itself is closer to solid body rotation, respectively. This result is in agreement with our previous finding where we showed that the MONDian rotation curve is not given by simply "inverting the density profile" as in the Newtonian case (cf. Fig. 9); the velocity in the outskirts of the halo is much larger and hence we expect a rise in $\lambda(r)$, too.

We are now going to focus on the shape of the halos. Firstly, we show measurements of the overall shape of halos and to this extent we calculated the eigenvalues $a > b > c$ of the inertia tensor. They were in turn used to construct the triaxiality parameter (e.g. Franx, Illingworth & de Zeeuw 1991):

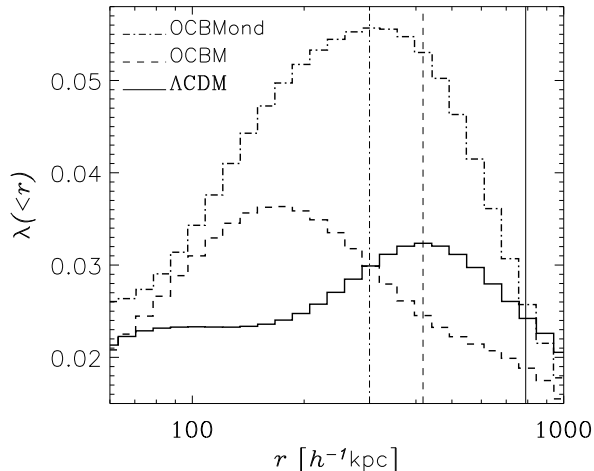


Figure 11. Radial distribution of spin parameter λ . The vertical lines are again showing the virial radius.

Table 3. Mean triaxiality parameter $\langle T \rangle$ and mean ellipticities $\langle e_1 \rangle$, $\langle e_2 \rangle$ when averaging over halos with $M > 10^{11} h^{-1} M_{\odot}$.

label	$\langle T \rangle$	$\langle e_1 \rangle$	$\langle e_2 \rangle$
Λ CDM	0.55	0.25	0.13
OCBMond	0.61	0.28	0.17
OCBM	0.55	0.21	0.12

$$T = \frac{a^2 - b^2}{a^2 - c^2}. \quad (19)$$

The triaxialities T are accompanied by the ellipticities

$$e_1 = 1 - \frac{c}{a}, \quad e_2 = 1 - \frac{b}{a} \quad (20)$$

and the values for the most massive object are summarized in Table 2. The mean values $\langle T \rangle$, $\langle e_1 \rangle$, and $\langle e_2 \rangle$ when averaging over all halos more massive than $10^{11} h^{-1} M_{\odot}$ can be found in Table 3. We observe a trend for the MOND halos to be more triaxial with higher ellipticities at the same time.

Secondly, we like to quantify subclumps within the virial radius of the halo itself. One possibility to measure the substructure content of a halo is to calculate the radial profile of the density dispersion

$$\sigma_{\delta}^2(r) = \frac{1}{N(r)} \sum_{i=1}^{N(r)} \left(\frac{\rho_i(r) - \langle \rho(r) \rangle}{\langle \rho(r) \rangle} \right)^2, \quad (21)$$

where $\rho_i(r)$ is the local density at a particle position which was estimated using the nearest 20 neighbors and $\langle \rho(r) \rangle$ the average taken over all $N(r)$ particles within a spherical shell $[r, r + dr]$. We used the same binning as already applied to the density profile and the rotation curve, respectively. The result for the most massive halo in all three runs is presented in Fig. 12. This figure shows that the dispersion is always smallest for the MOND halo, at least out to the virial radius: the density at each individual particle position is always close to the mean density. If there were subclumps present one would expect to find peaks in the $\sigma_{\delta}^2(r)$ curve due to local deviations from the mean density profile.

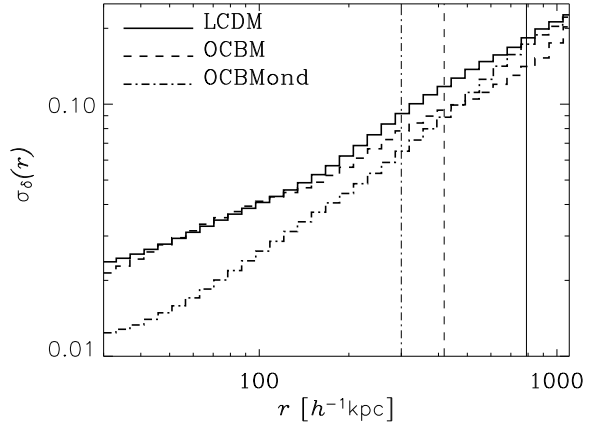


Figure 12. Variance $\sigma_{\delta}(r)$ for the most massive halo. The vertical lines are indicating the virial radius of the respective halo.

6 SUMMARY AND DISCUSSION

In this paper we presented three cosmological simulations: a fiducial standard Λ CDM model, a very low- Ω_0 model, and the same Ω_0 model but with MONDian equations of motions. Putting aside the classical arguments against MOND, we showed that structures found in a MONDian low- Ω_0 universe are not significantly different from the standard Λ CDM model. However, we derived several differences which might easily validate or rule out MONDian cosmologies observationally. Our main results can be summarized as follows:

- even though the OCBMond run was set up using a low value for $\sigma_8^{\text{norm}} = 0.4$ the simulation finished with $\sigma_8^{z=0} = 0.92$ (which is close to the cluster normalisation of the Λ CDM model),
- the OCBMond model shows an extremely fast evolution of the number density of halos for redshifts $z < 5$,
- virialized objects in a MONDian universe are slightly more correlated,
 - the density profile of MOND objects still follows the universal NFW density profile, but they are
 - far less concentrated,
 - show less substructure, and
 - are closer to solid body rotation.

We conclude that the most distinctive feature of a MONDian universe is the late epoch of galaxy formation; in a MONDian universe that is normalised to match a Λ CDM model at redshift $z = 0$ we expect to *not* observe any galaxies until recently ($z < 5$). This actually holds for any low- σ_8 universe either MONDian or Newtonian, but only the assumption of MOND can bring such a model into agreement with observations of the local universe again. Another interesting finding is that the outer parts of MOND halos are closer to solid body rotation than their standard Λ CDM counterparts even though the overall distribution $P(\lambda)$ is nearly indistinguishable from the Λ CDM model.

However, there have still been many assumptions made during the course of this study which are hard to justify and hence all results are to be understood simply as preliminary until our understanding of MOND actually improves. We not only assumed that MOND only affects peculiar ac-

Table 2. Properties of the most massive gravitationally bound object. The mass M is measured in $h^{-1} M_{\odot}$, velocities in km/sec and radii in h^{-1} kpc. χ^2 is actually the reduced χ^2 value as returned by IDL's `curvefit` routine.

model	M	σ_v	v_{vir}	r_{vir}	r_s	c	T	e_1	e_2	λ	λ_0	σ_{λ}	χ^2
Λ CDM	$5.6 \cdot 10^{13}$	657	553	790	91	8.7	0.65	0.30	0.18	0.025	0.040	0.53	0.8
OCBMond	$0.3 \cdot 10^{13}$	286	473	300	59	5.1	0.81	0.30	0.23	0.057	0.034	0.52	1.5
OCBM	$0.8 \cdot 10^{13}$	373	271	418	27	15.5	0.80	0.21	0.16	0.023	0.034	0.52	0.9

celerations in proper coordinates but also neglected the curl-term in Eq. (5). The effect of this rotational component is not clear, but it is guaranteed to decrease rapidly on large scales and vanish completely for objects that have spherical, planar or cylindrical symmetry. Another disclaimer is that MOND is based on the non-existence of dark matter, but our simulations only model gravity; if the universe consist only of baryons one definitely would need to include gas physics to be able to make credible predictions for internal properties of galaxies. But this is beyond the scope of this study. Nonetheless, we have shown that cosmology with MOND does not necessarily lead to completely odd results. Our treatment of MOND though gives clustering properties comparable to the favorite concordance Λ CDM model.

ACKNOWLEDGMENTS

The simulations presented in this paper were carried out on the Beowulf cluster at the Centre for Astrophysics & Supercomputing, Swinburne University. We acknowledge the support of the Australian Research Council through its Discovery Project program (DP0343508). We would like to thank the two anonymous referees for valuable comments that helped to improve the scientific content of the paper.

REFERENCES

Begeman K. G., Broeils A.H., Sanders R. H. 1991, MNRAS **249**, 523 (1991)
 Bahcall N. et al. , ApJ **585**, 182 (2003)
 Bekenstein J., Milgrom M., ApJ **286**, 7 (1984)
 Bento M.C., et al. Phys. Rev. D **62**, (2000)
 Bode P., Ostriker J.P., Turok N., ApJ **556**, 93 (2001)
 Brada R., Milgrom M., ApJ **519**, 590 (1999)
 Bullock J., Dekel A., Kolatt T.S., Kravtsov A.V., Klypin A.A., Porciani C., Primack J.R., ApJ **240**, 555 (2001a)
 Bullock J., Kolatt T.S., Sigad Y., Somerville R.S., Kravtsov A.V., Klypin A.A., Primack J.R., Dekel A., MNRAS **559**, 321 (2001b)
 Bullock J.A., astro-ph/0111005, 2001c
 Cole S., Lacey C., MNRAS **281**, 716 (1996)
 Colin P., Avila-Reese V., Valenzuela O., ApJ **542**, 622 (2000)
 Croft R.A.C. & Efstathiou G., MNRAS **267**, 390 (1994)
 Davis M., Efstathiou G., Frenk C.S., White S.D.M., ApJ **292**, 371 (1985)
 Dressler A., Shectman S.A., Astron. J. **95**, 985 (1988)
 Efstathiou G., Frenk C.S., White S.D.M., ApJ Suppl. **57**, 241 (1985)
 Frenk C.S., White S.D.M., Davis M., Efstathiou G., ApJ **327**, 507 (1988)
 Franx M., Illingworth G., de Zeeuw T., ApJ **383**, 112 (1991)
 Gardner J., ApJ **557**, 616 (2001)
 Gross M.A.K., PhD Thesis, Univ. California, Santa Cruz, 1997
 Qin B., Zou Z.L., A&A **296**, 264 (1995)

Klypin A.A., Holtzman J., astro-ph/9712217
 Knebe A., Müller V., A&A **354**, 761 (2000)
 Knebe A., Green A., Binney J., MNRAS **325**, 845 (2001)
 Knebe A., Devriendt J., Mahmood A., Silk J., MNRAS **329**, 813 (2002)
 Little B., Knebe A., Islam R.R., MNRAS in press, astro-ph/0205420 (2003)
 Maller A.H., Dekel A., Somerville R.S., MNRAS **329**, 423 (2002)
 Martel H., Matzner R., ApJ **530**, 525 (2000)
 Milgrom M., ApJ **270**, 365 (1983)
 Milgrom M., ApJ Lett. **496**, 89 (1998)
 Mortlock D.J., Turner E., MNRAS **327**, 557 (2001)
 Navarro J., Frenk C.S., White S.D.M., ApJ **490**, 493 (1997)
 Nusser A., MNRAS **331**, 909 (2002)
 Pinkney J., Roettiger K., Burns J.O., Bird C.M., ApJ **104**, 1 (1996)
 Power C., Navarro J.F., Jenkins A., Frenk C.S., White S.D.M., Springel V., Stadel J., Quinn T., MNRAS **338**, 14 (2003)
 Sanders R. H., ApJ **473**, 117 (1996)
 Sanders R.H., ApJ Lett. **512**, 23 (1999)
 Sanders R.H., ApJ **560**, 1 (2001)
 Sanders R. H., McGaugh S. S., Ann. Rev. A & A **40**, 263 (2002)
 Scarpa R., astro-ph/0302445 (2003)
 Scarpa R., astro-ph/0208061 (2002)
 Seljak U., Zaldarriaga M., ApJ **469**, 437 (1996)
 Spergel D.N., Steinhardt P.J., Phys. Rev. Lett. **84**, 3760 (2000)
 Spergel D.N., et al. astro-ph/0302209
 Swaters R. A., Madore B. F., van den Bosch F. C., Balcells M., ApJ **583**, 732 (2003)
 Warren M.S., Quinn P.J., Salmon J.K., Zurek W.H., ApJ **399**, 405 (1992)

This figure "Fig1.jpg" is available in "jpg" format from:

<http://arxiv.org/ps/astro-ph/0303222v2>

This figure "Fig6.jpg" is available in "jpg" format from:

<http://arxiv.org/ps/astro-ph/0303222v2>